

Design and optimization of Metallic Foam Shell protective device against flying ballast impact damage in railway axles

Gabriella Epasto^a, Fabio Distefano^a, Linxia Gu^b, Hozhabr Mozafari^b, Emanoil Linul^{c,*}

^a Department of Engineering, University of Messina, Messina, Italy

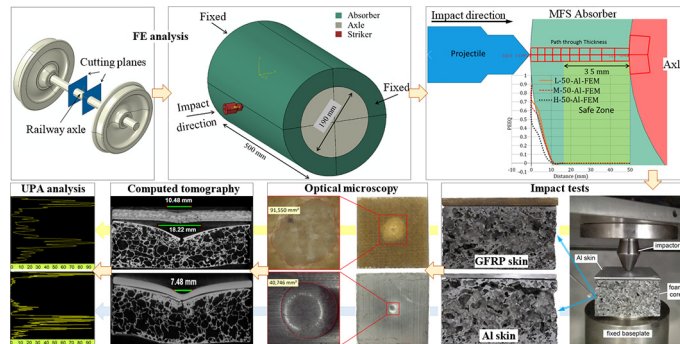
^b Department of Mechanical Engineering, University of Nebraska-, Lincoln, NE, USA

^c Department of Mechanics and Strength of Materials, Politehnica University of Timisoara, Timisoara, Romania

HIGHLIGHTS

- A novel Metallic Foam Shell (MFS) protective device against flying ballast impact damage in railway axles is designed.
- By using impact tests and non-destructive evaluation methods, the most optimal MFS configuration is proposed.
- The newly developed MFS device can absorb up to 90% of the initial impact energy with total protection of the axle.
- The suggested MFS device can be effectively evaluated by means of the most common non-destructive techniques.

GRAPHICAL ABSTRACT



ARTICLE INFO

Article history:

Received 11 July 2020

Received in revised form 28 August 2020

Accepted 2 September 2020

Available online 03 September 2020

Keywords:

Protective sandwich structure

Railway axle

Ballast impact behaviour

Non-destructive evaluation

Finite element analysis

ABSTRACT

Ballast impacts can initiate surface defects that cause abrupt failure of the axle and derailment of the railway vehicle. According to the Federal Railroad Administration the axle and bearing failure costs around 89 million dollars and causes 46 derailments in the US per year (2005–2010). In this study, the authors have suggested a novel protective mechanism (Metallic Foam Shell – MFS) by using a lightweight sandwich panel. At the first step, a preliminary study is conducted, followed up by the numerical simulations to determine the applicable materials. At the next step, experimental tests were performed to assess the efficiency of the suggested device against flying ballast impacts. An extended non-destructive (NDT) evaluation has been performed in order to find the most suitable technique for damage detection of the proposed device when on-service. The studied cases were GFRP and Aluminium sandwich panels, having an aluminium foam core with different densities and thicknesses. The results showed that the MFS can absorb up to 90% of the initial impact energy and significantly decrease the chance of rebounding impact to the other components. Moreover, the results were also analysed in order to propose the most reliable NDT method for this specific application.

© 2020 The Authors. Published by Elsevier Ltd. This is an open access article under the CC BY license (<http://creativecommons.org/licenses/by/4.0/>).

1. Introduction

Railway axles are known as the most loaded parts in the railway vehicles since they account for about 70% of wagon mass. Axles are

designed against endurance limit [1]. However, formation of crack and failure significantly decreases their fatigue life. According to the Federal Railroad Administration (FRA) in 2005–2010, the axle and bearing failure costs around 89 million dollars and causes 46 derailments per year in the US [2].

Two main axle failure mechanisms are overheating of the roller bearing, known as ‘hot box’ [3] and fatigue from sub-surface and surface

* Corresponding author.

E-mail address: emanoil.linul@upt.ro (E. Linul).

Nomenclature

CLT	Classical Lamination Theory
CT	Computed Tomography
Dx	Flexural stiffness along x axis (N·mm)
E	Young's modulus (MPa)
E_{ad}	Energy absorption (J)
E_i	Impact energy (J)
F_{max}	Impact max force (N)
GFRP	Glass Fibre Reinforced Polymer
MFS	Metallic Foam Shell protective device
PEEQ	Equivalent plastic strain
PT	Pulsed Thermography
SAE	Specific Absorbed Energy (J/kg)
T_{core}	Core thickness (mm)
T_{skin}	Skin thickness (mm)
UPA	Ultrasonic Phased Array
VT	Visual Testing
w	Displacement (mm)
ϵ_{max}	Elongation at break (%)
ρ	Density (kg/m ³)
ρ_{core}	Core density (kg/m ³)
σ_y	Yield stress (MPa)

defects, predominantly initiating at corrosion pits [4] and nucleated micro-cracks [5]. These micro-cracks initiate from ballast impacts, typically small, sharp gravel particles or pebbles from the sleeper beds of railway tracks [6]. In Australia, a high-speed train derailed in 2006 due to micro-cracks that nucleated at depth of 0.1–0.9 mm from ballast impact on the surface of the axles [6]. In the same year, other 12 railway axles failed due to the similar type of defects [6]. In July 2008, a high-speed train derailed in Cologne, Germany, due to the combined effects of non-metallic inclusions and corrosion at the pressed fit section of the T-junction on the axle, causing the failure of the axle [7].

It is well known that the most common reason for crack initiation and corrosion pits is flying ballast [8]. The flying ballast occurs when a combination of both mechanical and aerodynamic forces, generated mostly by the passage of the train, cause one or more ballast particles to overcome gravity. It is reported that 30% of the high-speed axles were affected by flying ballast impacts [8]. Of course, a ballast-induced notch is not a crack although there is some chance of sharp edges from which small fatigue cracks could easily develop. Flying ballast can affect the safety of staff working along the railway lines, train safety and, consequently, passengers, or impose financial loss to the railway vehicle and the infrastructure maintenance [9]. Since no regulation is defined by international standards about flying ballast, implementing a method to protect the vehicle axle can control the inflicted damages to the rolling stocks and decrease the maintenance costs.

One of the first solutions was provided by Murphy et al. [10] by introducing a protective device for a drive shaft of a front-wheel drive of a tractor. The device consists of two holders fixed on the gearbox housing and the housing. The holders and entire shaft were then encircled with a protective tube encircling. The mechanism was improved by Kontio et al. [11] by altering the protective device to a circular-cylindrical pipe consisting of an inner and outer layer. The inner one was made of a foamed plastic and glued to the outer layer and the whole system was fastened to the axle. The installation process was faster than the previous method although the tight connection against the axle led to trapping moisture between the inner layer and the axle. The rusts created due to moisture could trigger corrosive reactions and damage the axle. To overcome this issue, an excel version of the previous design was proposed by Tolérus and Lundhammar by adding some radial gaps and elongate the ridges which formed an air channel between the cover and the axle [12]. A less expensive technique was

proposed by Chretien et al. [13] where the axle was protected by a polymer strip with an uncomplicated assembly process. The application of the mentioned protective systems was limited to the axle classes which depends on the rolling stock speed. A protective system, which could be implemented to rolling stock independently to the class and facilitate the inspection of the axle was presented by Guenard and Thouvenot [14]. The system consisted of two or three layers of different materials. The first layer was capable of adhering to the axle. The second layer comprised at least one adhesive compound in pasty form adhered to the first layer. Depending on the axle class, the third layer could be implanted. Moreover, using special adhesives and different layers of protection could improve the impact absorbing properties. However, the designed system could not completely protect the axle against the flying ballast due to the lack of impact resistance. Therefore, the outer layer was substituted with a relatively hard shielding layer to resist against ballast impact without failing and a flexible inner layer as a shock absorber [15]. Another protection device was proposed by Dohn and Jensen [16] to fulfil axle protection against flying ballast, grit, and chunk of ice while preventing corrosion. The protective device had a substantially tubular shape, comprised a shell and spacers which created a gap between the shell and the axle that played as an anti-corrosion system. The gap and the rotation of the wheel led drainage of the condensed water. The device could be easily removed for a safer maintenance and inspection. On the other hand, this system was adoptable for a specific designed geometry, which could increase the manufacturing cost. Afterwards, in the new design, a two half shells protective device was manufactured by adding the elastomer strips [17]. Based on the axle diameter, correct elastomer thicknesses could be selected and implemented in the device. Accordingly, the manufacturing costs for making shells with different diameters were eliminated. The performance of developed devices was affected by climate factors such as temperature, which could alter the elastic properties and the thickness of the elastomer layer. Additionally, the designed devices did not cover the entire wheelset and the uncovered areas could be exposed corrosion and axle failure [18]. To solve this issue, a protective covering technique was applied to the metal surface of the wheelset. The added layer consisted of three painting sub-layers to provide adhering properties and to protect the wheelset against ballast impacts [18]. Although the protective layers were not subjected to softening at higher temperatures, the visual inspection of the axle surface became infeasible. Also, the maintenance was more laborious and expensive since the coating must be repaired locally.

In this paper, the authors have developed a novel axle protective device, named Metallic Foam Shell (MFS), to overcome the main drawbacks of the conventional devices. Among the potential materials, it was decided to implement a lightweight sandwich panel as the integrated structure of this novel ballast impact absorber. At the first step, a preliminary study is conducted which then followed up by numerical simulations to determine the applicable materials. At the next step, experimental tests were performed to assess the efficiency of the MFS against flying ballast impacts. An extended non-destructive (NDT) evaluation by means of visual testing (VT), computed tomography (CT), ultrasonic phased array (UPA), pulsed thermography (PT) has been performed in order to find the most suitable technique for damage detection of the device when on-service. Gaudenzi et al. [19] compared different NDT techniques to assess impact damage on carbon fibre/epoxy laminates, finding that transient thermography underestimates damage extension respect to UPA results. Also, the results of UPA with X-ray CT to assess the misestimation respect to the true damaged area due to impact in carbon fibre-reinforced composite specimens were compared by Katunin et al. [20].

The proposed MFS can absorb impact energies through inelastic deformation, which is advantageous in terms of minimizing the rebounding of the ballast stones and impact recurrence. Moreover, installation can be conducted through a fastening mechanism, which allows an uncomplicated disassembly of the device for the scheduled

inspections of the axle. In addition, there is no need to increase the roughness of axle, as the attachment of the MFS is not based on adhesives. Finally, the MFS can be used effectively within a wide temperature range, which will allow the railway administration to avail the device within harsh climate conditions. In selecting the most suitable material for the final design of the MFS, particular attention was made to the environmental aspect for the disposal of the device at its out-of-service. Thus, a fully recyclable material is proposed.

2. Materials and methods

2.1. Materials and sample preparation

The common and lightweight cores have open-cell or closed-cell structures such as polymeric and metallic [21–23] foams. These materials have unique mechanical properties, which make them interesting for a variety of structural engineering applications. Among the different available polyurethane [24] and metal [25–27] foams, the authors chose closed-cell aluminium foams. These materials have interesting combinations of properties such as high stiffness, strength combined with high-energy absorption capacity, and formability. These features guide us to choose these foams as the potential elements of the MFS [28].

2.1.1. Materials

Large foam panels with different densities were prepared by powder metallurgical (PM) route, based on AlSi10 alloy. The chemical composition of the metallic foam was 10 wt% Si and Al balanced, while 0.4 wt% of titanium hydride (TiH_2) powder was used as foaming agent via heating up to 620 °C. Following the PM process, closed-cell aluminium foam panels with densities in the 550–1300 kg/m³ range were obtained. Except the thickness, where 20- and 34-mm thicknesses were imposed, all panels had the same in-plane dimensions (500 mm × 500 mm).

Among the available metallic and non-metallic sheets materials, the authors decided to choose Glass Fibre Reinforced Polymer (GFRP) composite and aluminium alloy 6082 for the skin of sandwich panels (Fig. 1a, b). GFRP composites are part of lightweight materials with high strength-to-weight ratio and resistant to environmental conditions (saltwater, chemicals, acid rain, salts and most chemicals), while Al alloy 6082 highlights crushing performances, excellent corrosion resistance, low cost and good formability.

The main physical and mechanical properties of GFRP and aluminium skins are described in Table 1. The mechanical properties of GFRP skins were calculated by tensile tests on rectangular samples with tabs and are consistent to such found in literature [29].

The GFRP skins were produced by using bi-directional fabrics in 0°/90° directions, and MAT type fibres. The bi-directional fabrics had a specific weight of 400 g/m² and MAT fabrics had a specific weight of 225 g/m². The fibre volume fraction was 0.55.

2.1.2. Sample preparation

For performing quasi-static compression tests, from the obtained panels, cubic foam samples with thickness of 20 mm and 34 mm were prepared. In order to obtain accurate samples and to prevent any damage to the cellular structure, a non-traditional Electric Discharge Machining cut the foam samples. Fig. 1c presents the large foamed panel, while Fig. 1d shows the cut samples used for impact tests.

Twelve samples with various foam density, thickness and face-sheet materials was produced to be used in the impact tests. In-plane dimensions of the samples were 60 mm × 60 mm with the out-of-plane dimension of 20 mm and 34 mm as the two groups with different thicknesses. The face-sheet materials were aluminium alloy and GFRP, Fig. 1e and f. The produced samples are listed in Table 2.

The thickness of aluminium skin is 2 mm that was evaluated in order to obtain the same flexural stiffness values in x and y directions of the GFRP with 4.3 mm thickness. The flexural stiffness D of the GFRP was calculated by applying both Classical Lamination Theory (CLT) and

Dietz approach [31]. The obtained values were $D_{x,CLT} = 56.79 \cdot 10^3 \text{ N} \cdot \text{mm}$ by Classical Lamination Theory and $D_{x,Dietz} = 56.76 \cdot 10^3 \text{ N} \cdot \text{mm}$ by Dietz approach. The mean value is $D_x = 56.77 \cdot 10^3 \text{ N} \cdot \text{mm}$.

By applying the Kirchhoff-Love theory of plates [32], the aluminium thickness which allows to obtain the same flexural stiffness value of the GFRP skin, was evaluated as 2.113 mm. Whereas aluminium layers commercially available present values of 2 mm or 2.5 mm; authors chose 2 mm thickness, which present a flexural stiffness of $52.4 \cdot 10^3 \text{ N} \cdot \text{mm}$.

2.2. Experimental set-up

2.2.1. Preliminary quasi-static tests

Quasi-static compression tests were performed according to the ISO 13314-2011 standard [33]. The experiments were carried out on a 100 kN LBG TC100 universal testing machine, by using a constant nominal crosshead speed of 10 mm/min. The compressive load and the crosshead displacement were recorded during the tests by using a software embedded in the test machine. The tests were performed at room temperature under normal humidity conditions.

2.2.2. Low-velocity impact tests

The low-velocity impact tests were performed with a Ceast Fractovis Plus drop test machine, equipped with a system for the elimination of multiple impacts. Impact energy can be varied by adjusting the impactor mass and the drop height. The machine is provided with a spring system, which is automatically activated when the tower height is insufficient to obtain the requested potential energy. The testing conditions follow the NF F07-101 standard [34], which defines foam-based composite damage resistance for low velocity impacts in railway applications. The tests were carried out with an impacting mass of 5.46 kg, an impact velocity of 3.58 m/s and a drop height of 0.65 m corresponding to an impact energy of 35 J and the K4 class [34] (according to railway standard). The impactor used for the tests complies with ASTM D5628 Method FB [35] with the geometric parameters shown in Fig. 2a, and it hits the samples at the centre point.

The critical outputs were the energy absorption capability, integrity of the structure, and the rebounding of the impactor. Fig. 2b shows the impact setup test and a sandwich sample.

2.2.3. Non-destructive inspection

Non-destructive inspection was carried out in order to analyse the damage occurred on the sandwich samples during impact test: VT, CT, UPA, PT were performed and the difference between the results were also analysed in order to propose the most reliable method for this specific application.

Computed Tomography analyses were carried out by an industrial CT equipment (Y.CT Vario) equipped with a multi-focal source and a 3D reconstruction software analysis (VGStudio Max 2.0). The scans were performed with a 200 µm focal spot size; voltage and current were set to 200 kV and 1 mA, respectively. A Cu beam filter having a thickness of 1 mm was put between the source and the sample. For the reconstruction, a voxel resolution of $46 \times 46 \times 46 \mu\text{m}$ has been chosen, with a pixel resolution in tomogram of 2048×2048 .

Ultrasonic phased array tests were performed by using Olympus Focus PX 16/128 acquisition unit with integrated Tomovision software and a 64 elements linear probe @ 3.5 MHz (3.5 L64-NW1, 64 mm aperture, 1 mm pitch, 7 mm elevation) equipped with a wedge SNW1-0 L-IHC and with a VersaMOUSE encoder (see Fig. 3a).

The inspection was performed for both types of sandwich structures object of the study. More in detail, the sandwich with GFRP skin presented the difficulty to detect the damage from visual inspection and the different material velocity longitudinal waves between GFRP skin and the aluminium core, which gives high attenuation of ultrasonic waves. For the last reason, the inspections were performed only for the skins. For sandwich with aluminium skin, the inspections were

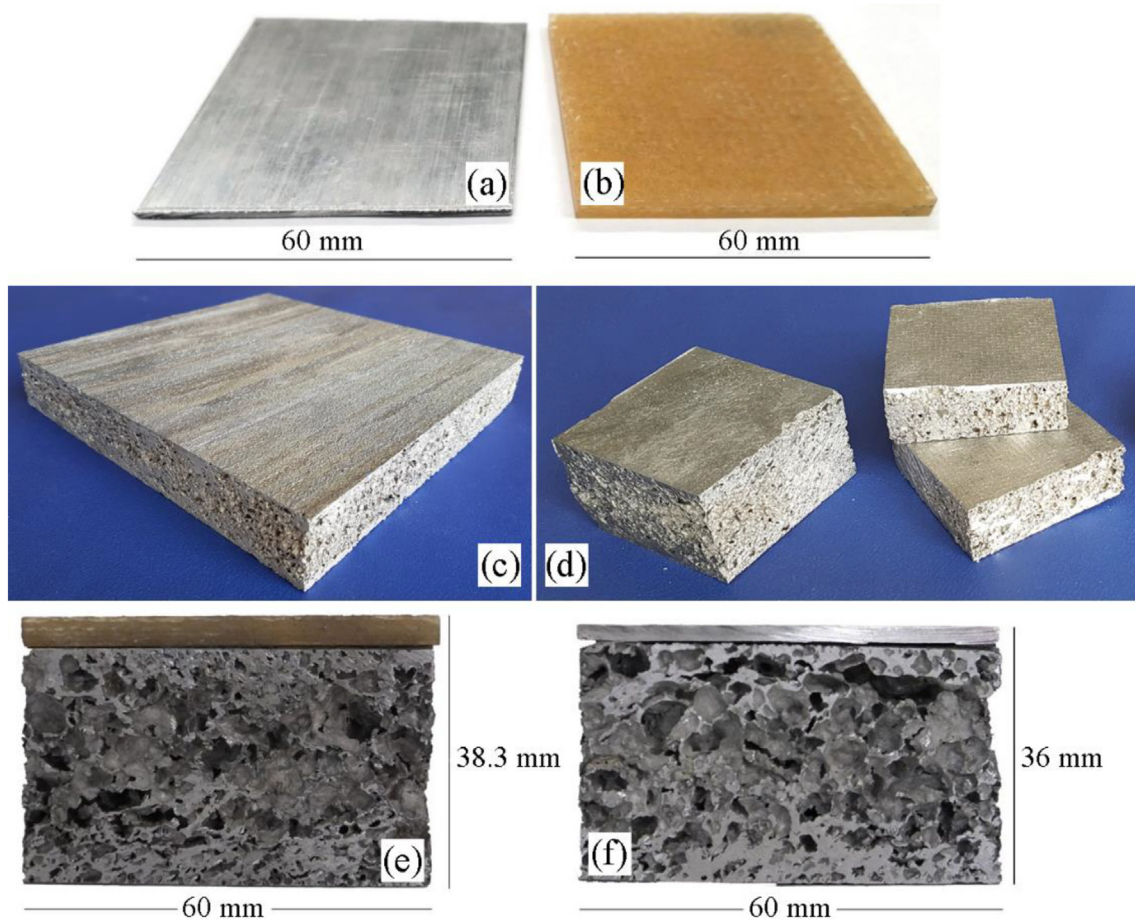


Fig. 1. The aluminium (a) and GFRP (b) sheets for preparing the sandwich panel skin; Large foamed panel (c) and prepared samples for impact tests (d); The cross section of sandwich samples with core thickness of 34 mm: GFRP (e) and aluminium (f) skins.

Table 1
Mechanical properties of GFRP and aluminium alloy 6082 [30].

Material	ρ (kg/m ³)	E (MPa)	σ_u (MPa)	ϵ_{max} (%)
GFRP	1328	7500	80	1.3
Aluminium	2700	70000	385	10

Table 2
Summary of the samples produced for the impact tests.

Skin material	Sample code	ρ_{core} [kg/m ³]	T_{core} [mm]
Aluminium	L-20-Al	490	20
	M-20-Al	570	
	H-20-Al	690	
	L-34-Al	490	34
	M-34-Al	570	
	H-34-Al	690	
GFRP	L-20-GFRP	490	20
	M-20-GFRP	570	
	H-20-GFRP	690	
	L-34-GFRP	490	34
	M-34-GFRP	570	
	H-34-GFRP	690	

Legend: L (Low, 490 kg/m³), M (Medium, 570 kg/m³), H (High, 690 kg/m³) represent core density; 20 and 34 are core thickness; Al and GFRP are skin materials.

conducted over the whole sample (i.e. skin plus core). Thus, longitudinal wave velocity was calculated: for the GFRP 2757 m/s was obtained, while for aluminium 4223 m/s. Phased array calibrations were performed by adjusting beam delay and sensitivity; for both cases, the beam delay was adjusted in order to match the front wall with the zero point. Sensitivity parameters obtained from the calibration are the following: for the GFRP the reflector amplitude was 100% with a tolerance of 10% and a gain of 20 dB; while for the aluminium the reflector amplitude was 90% with a tolerance of 5% and a gain of 26 dB. The encoder resolution was also calibrated: value obtained for GFRP was 8.55 steps/mm, while for aluminium 9.07 steps/mm. UPA inspections have been carried with a resolution of: 1 pixel = 1 mm.

Pulsed Thermography analyses were carried out only on the samples having GFRP skins, due to the difficulties to reach reliable results on aluminium skins. The thermograms were recorded using a Flir Systems SC640 thermal camera, with a resolution of 640 × 280 pixels and having thermal sensitivity of 30 mK @ 30 °C. The Infrared (IR) thermal camera is equipped with Focal Plane Array (FPA) uncooled microbolometer sensor. The frame rate was set to 60 fps. The thermograms were post-processed with FLIR Thermacam Research Pro software. The Rainbow palette was considered the most suitable for the analyses of the present study. The samples were black painted with acrylic enamel. The thermal camera was placed on a tripod at a distance of 0.4 m from the sample; the instant field of view (IFOV = 0.26 mm) was calculated for the mounted IR lens, having focal length 38 mm at a distance of 0.4 m from the target. The flash was placed near the camera (Fig. 3b). In

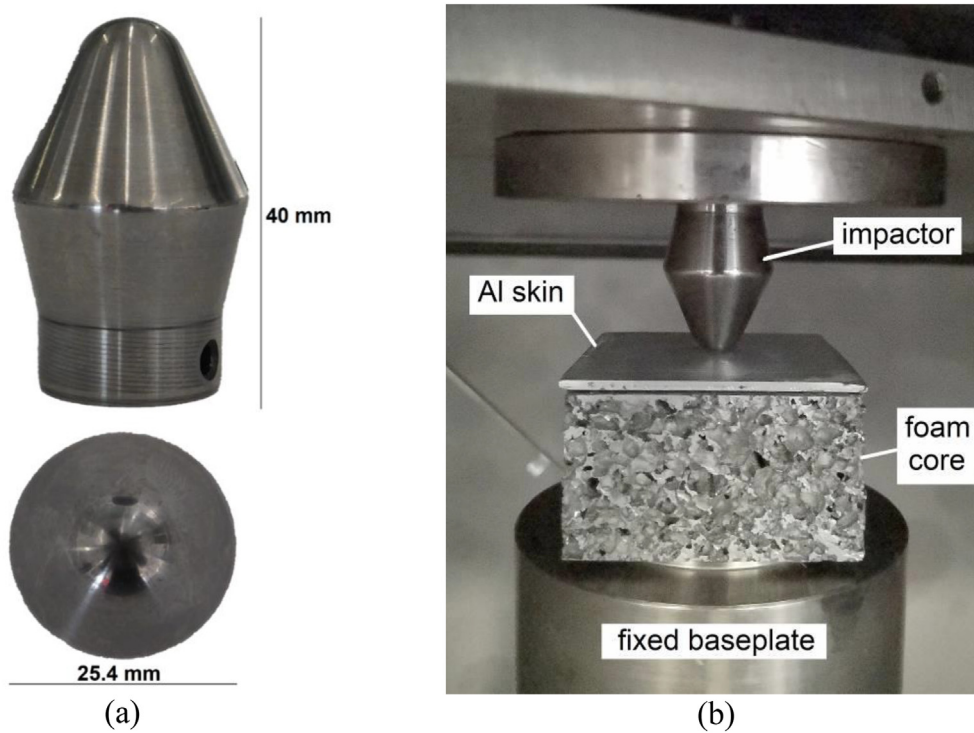


Fig. 2. (a) Conical shape impactor: 6.35 mm conical radius and $\varnothing 25.4$ mm base; (b) The impact test setup.

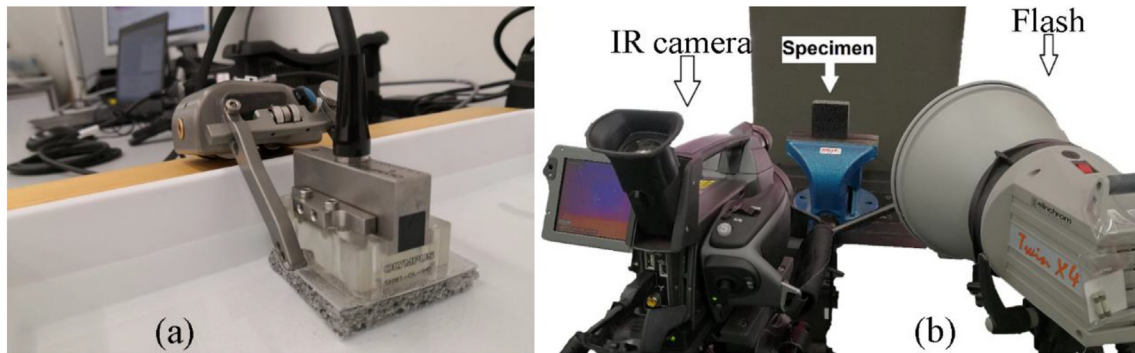


Fig. 3. (a) UPA set-up and position of the probe on the sample. The analyses were performed in water (immersion technique). (b) PT set-up.

order to propose this technique for on-site inspections, a handled camera was chosen, and no signal processing has been performed after recording (i.e. no lock-in algorithm was applied). Flash and IR camera were manually triggered, in order to allow also non-expert employers to perform the test in a very simple and fast way.

2.3. Finite element simulation

Finite element (FE) models were developed for two objectives. The first one is to simulate the quasi-static compression tests in order to validate the modelling of the foam by importing the mechanical properties obtained from the experimental tests. The second one is to measure the performance of the MFS against impact and evaluate the optimum thickness of the absorber.

The 3D FE model of the foam is developed by using ABAQUS® software package. Crushable foam behaviour was considered to include the hardening effect due to the compression. The authors have implemented this technique in their previous works [36,37]. The stress-strain curves from experiments have been used to calibrate the

CRUSHABLE FOAM HARDENING material model. This model with isotropic hardening was developed by Deshpande and Fleck [38] has been used to simulate the plasticity of the aluminium foam in compression. The hardening model in ABAQUS®/Explicit uses a yield surface that is ellipse centered at the origin in the $p - q$ stress plane. According to the material model, the yield function is:

$$f = \sqrt{q^2 + \alpha^2 p^2} - B \quad (1)$$

$$g = \sqrt{q^2 + \beta^2 p^2} \quad (2)$$

where

B defines the size of the yield ellipse, p and q are the pressure and the Von Mises stress, respectively. The yield surface represents the Von Mises circle in the deviatoric stress plane, and the flow potential is an ellipse centered at the origin. The shape factor α can be computed using the initial yield stress in uniaxial compression, σ_0^c and the initial yield stress in hydrostatic compression, p_0^c using the relation:

$$\alpha = \frac{2k}{\sqrt{9-k}} \quad (3)$$

$$k = \frac{\sigma_0^c}{p_0^c} \quad (4)$$

where k is the yield stress ratio. For a valid surface, the choice of the yield stress ratio must be in range 0–3. For many low-density foams, the initial yield surface is close to a circle in the $p - q$ stress plane, which indicates that the value of α is approximately equal to unity. Parameter β (the shape of the flow potential ellipse on the $p - q$ stress plane) for the isotropic hardening model is defined as:

$$\beta = \frac{2}{\sqrt{2}} \sqrt{\frac{1-2\vartheta_p}{1+\vartheta_p}} \quad (5)$$

The plastic Poisson's ratio ϑ_p , which is the ratio of the transverse to the longitudinal plastic strain under uniaxial compression, must be in the range between 1 and 0.5 [38]. For many low-density types of foams, the plastic Poisson's ratio ϑ_p is near zero, which corresponds to a value of $\beta \approx 2.12$. Assuming that Poisson's ratio is equal to zero, two parameters are needed to set the initial ellipse. These could be the initial yield stress in uniaxial compression, σ_0^c initial yield stress in hydrostatic compression, p_0^c . Parameter σ_0^c is the stress value at the initiation of plastic regime. Here the value of k is assuming to unity in eqs. (3) and (4). The corresponding value of β can be determined and then p_0^c is estimated.

The model associated with compression test included three parts: the foam, the stationary plate, and the moving plate. The moving plate was constrained to move only in the perpendicular axis with respect to the foam face. The mechanical properties of the foam were imported from the conducted experimental tests. The simulations were carried out by explicit solver while tracking the kinetic energy versus total energy of the model to ensure the quasi-static condition of the model. Mesh sensitivity analyses were performed, and the model was meshed with an element size of 2 mm.

The FE impact model consists of the absorber, the striker and the axle. According to NF F07–101 standard and K4 class, the impact scenario for the ballast with impact energy of 35 J was simulated. Due to the local effect of ballast impact, two cutting planes were used to take a section of axle and, then, applied symmetrical boundary conditions at both ends (Fig. 4a and b). The dimensions of the axle were obtained from [39], Fig. 4b.

The total thickness of absorber was 50 mm and the thickness of skin was 2.5 mm. The total number of nodes was 167,925 and the total number of elements was 164,220, which included 13,000 linear quadrilateral S4R and 151,220 linear hexahedral C3D8R elements. The both ends of axle were constrained in all degrees of freedom. The striker was modelled by using rigid body feature and the point mass applied to its centroid. The magnitude of velocity was adjusted to provide kinetic

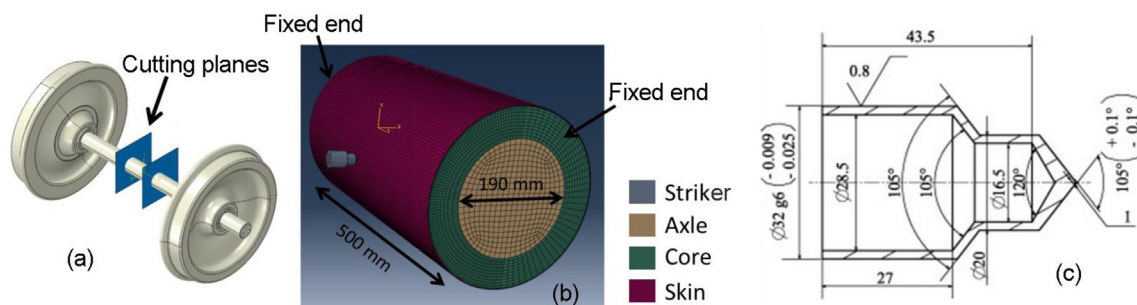


Fig. 4. Finite element model of the impact analysis; (a) Railway axle model and the cutting planes; (b) the selected section of the axle covered with the MFS; (c) The dimension of striker (mm).

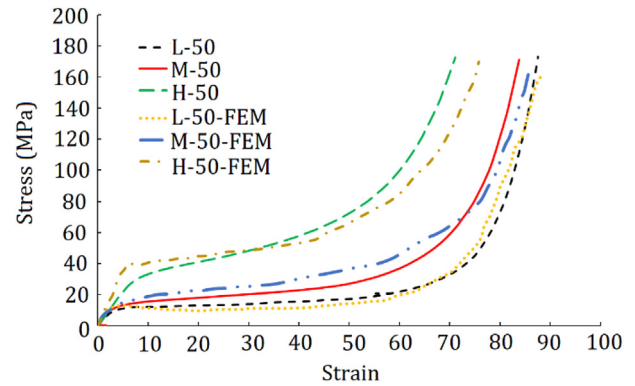


Fig. 5. The quasi-static stress-strain diagram of aluminium foam cores.

energy of 35 J. The low velocity impact of lightweight sandwich panels can be modelled as a quasi-static event in which the strain rate effects are negligible [40,41]. Therefore, we did not include the strain rate as an input in our modelling. The axle was modelled as elastic perfectly plastic material. The model was meshed with 3D solid elements.

The impact region was meshed with more refined mesh for the sake of accuracy and mesh sensitivity analysis was performed to obtain the optimum element size. Surface to surface contact was applied between the striker and the MFS. Based on our previous observations with impact tests and the strength of applied epoxy, the adhesive bonding between the skin and the core of MFS was considered to be perfect, and surface-based tie constraint was adopted at the skin–core interface [42]. By implementing tie constraint, each node of the core at the interface was constrained to have the same translational and rotational motion at the node on the skin. The tie constraint disallowed surfaces initially in contact from penetrating, separating or sliding relative to one another. Moreover, the tie constraint was applied between the MFS and axle to simulate clamping mechanism.

3. Results and discussions

3.1. Preliminary quasi-static results

The mechanical response of the foams was obtained by using quasi-static compression tests. For each case, 3–5 tests were performed, and the average response was considered. The naming of samples was based on their density. Based on the data collected by the electromechanical computerized testing machine software, the load-displacement curves were obtained. Further, by using the geometrical parameters of the samples (width, length and height), the load-displacement data were converted to stress-strain curves. Fig. 5 shows the stress-strain curves obtained during the compression tests for each foam.

Table 3

Main physical and quasi-static mechanical properties of investigated foams.

Core Code	Young's modulus (MPa)	Yield Strength (MPa)	Plateau Stress (MPa)	Densification Strain (%)	Densification Stress (MPa)	Energy Absorption (MJ/m ³)	Poisson's ratio [40] (–)
L-50	288.43	12.27	14.38	54.26	18.69	7.49	0.2663
M-50	392.77	14.54	20.47	49.28	26.62	9.21	0.2857
H-50	462.19	32.67	49.40	45.01	64.22	18.51	0.3105

The stress-strain curves highlight a behaviour characteristic of cellular materials and present three distinct regions, namely linear-elastic, plateau and densification region [43–50]. The first region can be found up to 5% strain for all investigated densities. The length of the plateau region differs significantly depending on the density of the foam. Thus, it is observed that for low density the plateau ranges from 5 to 55% strain, while for high density it reaches only up to 45% strain. Due to the collapse mechanisms (yielding, fracture and bending of cell faces/walls, buckling phenomenon, etc.) that occur in the foam structure, all curves show an obvious hardening of the plateau region [51–54]. Finally, the densification region begins with the completion of the plateau region and ends with the completion of the test. At the end of this densification region, the cells come into direct contact with each other, and the foam begins to behave as a solid material (more precisely than the solid material from which they are made) [55–59].

The main physical and quasi-static mechanical properties of tested foams in preliminary stage are listed in Table 3.

The main investigated mechanical properties increase polynomially with increasing foam density. At a density increase of 1.32 times, the growth of properties is relatively small (under 30%), while at a slightly higher increase of only 1.57 times, most doubles (especially the strength properties and energy absorption capabilities).

3.2. FE results

After choosing the constituents of the sandwich panel, the authors needed to estimate the total thickness of the absorber which according to the Railway tolerance standard must be less than 50 mm [60]. It is worthy to mention that in our developed FE model; only the aluminium skin was modelled as the face sheets of the sandwich panel. The authors wanted to first observe the responses of this material in simulations, which was our prior choice due to its recyclability.

One of the critical parameters is the plastic deformation. This parameter shows that the permanent indentation and the irreversible

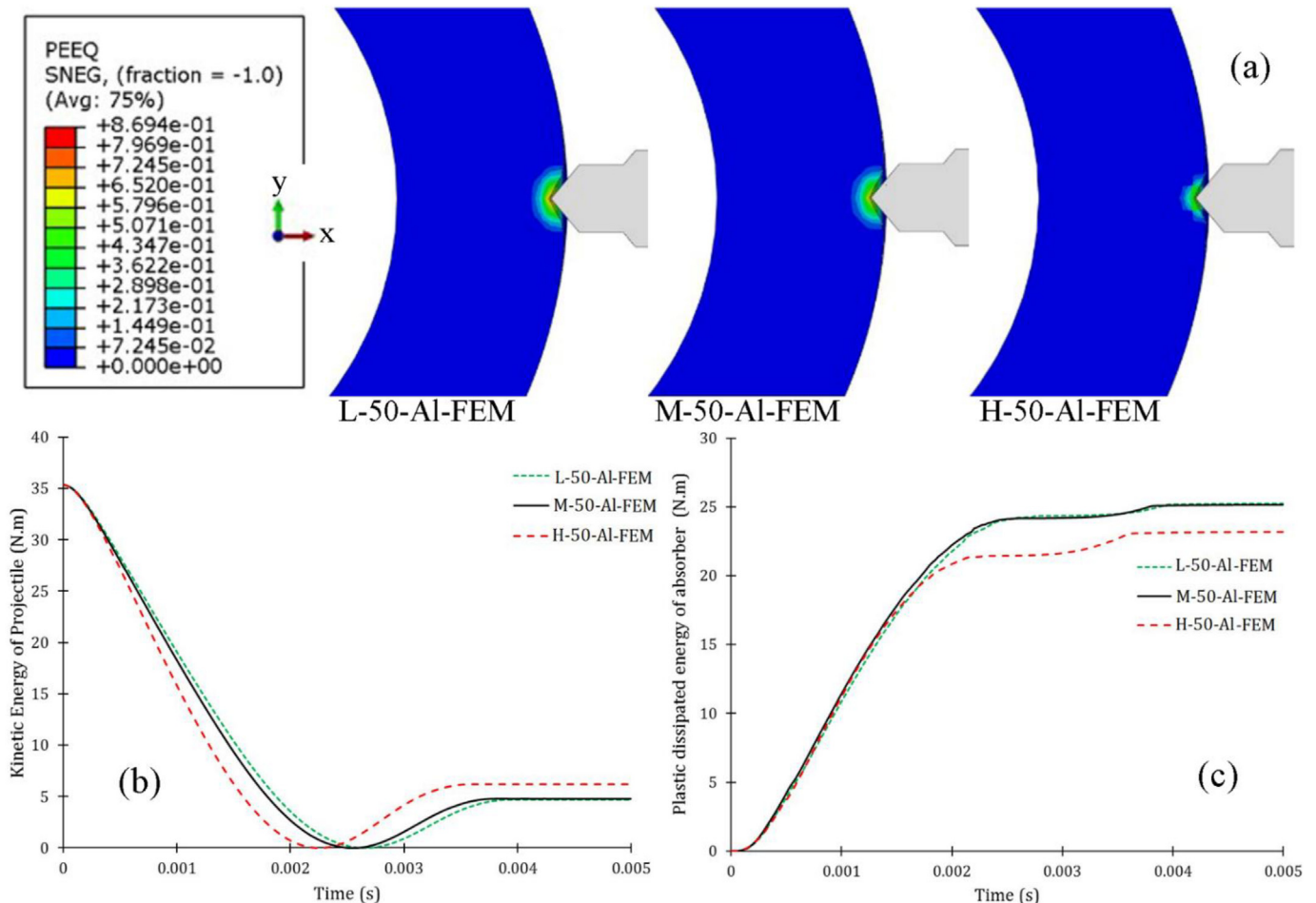


Fig. 6. (a) Equivalent plastic strain (PEEQ) for each case after the impact; (b) Kinetic energy of the projectile during the impact simulation; (c) Plastic dissipated energy during impact.

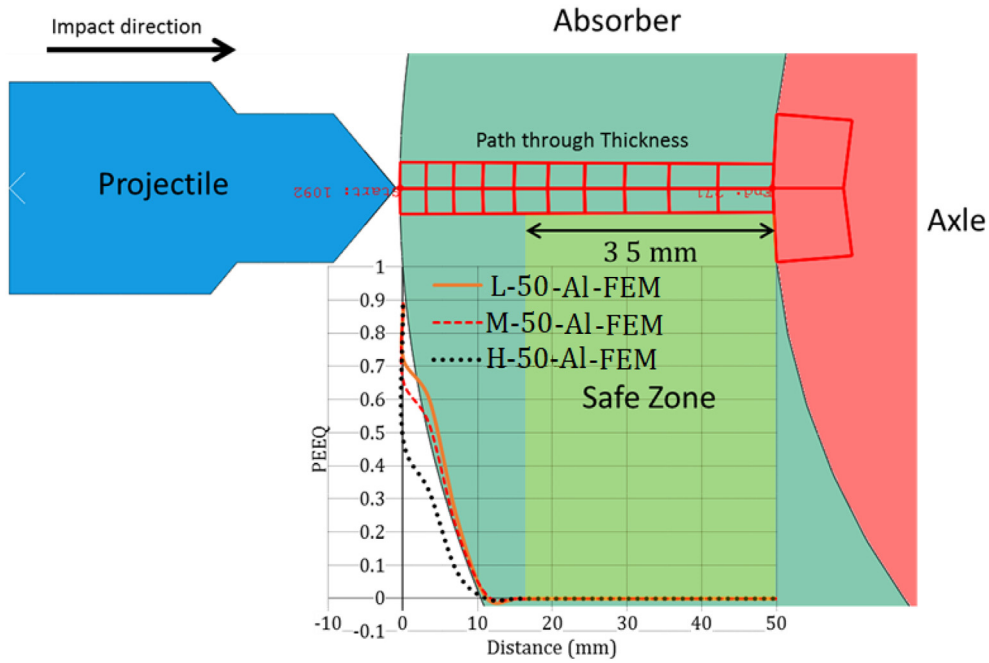


Fig. 7. PEEQ variation through the thickness of absorber.

deformation is induced by projectile impact. Fortunately, in none of the cases fully plastic deformation was observed. In other words, a portion of deformation was elastic which is a reversible deformation [61,62]. Fig. 6a shows the equivalent plastic strain for each case. The least plastic

deformation is for the absorber with H-50-Al due to its higher strength; although the difference among the three types was less than 6%. Unlike the conventional rubber systems or coating mechanisms, the MFS

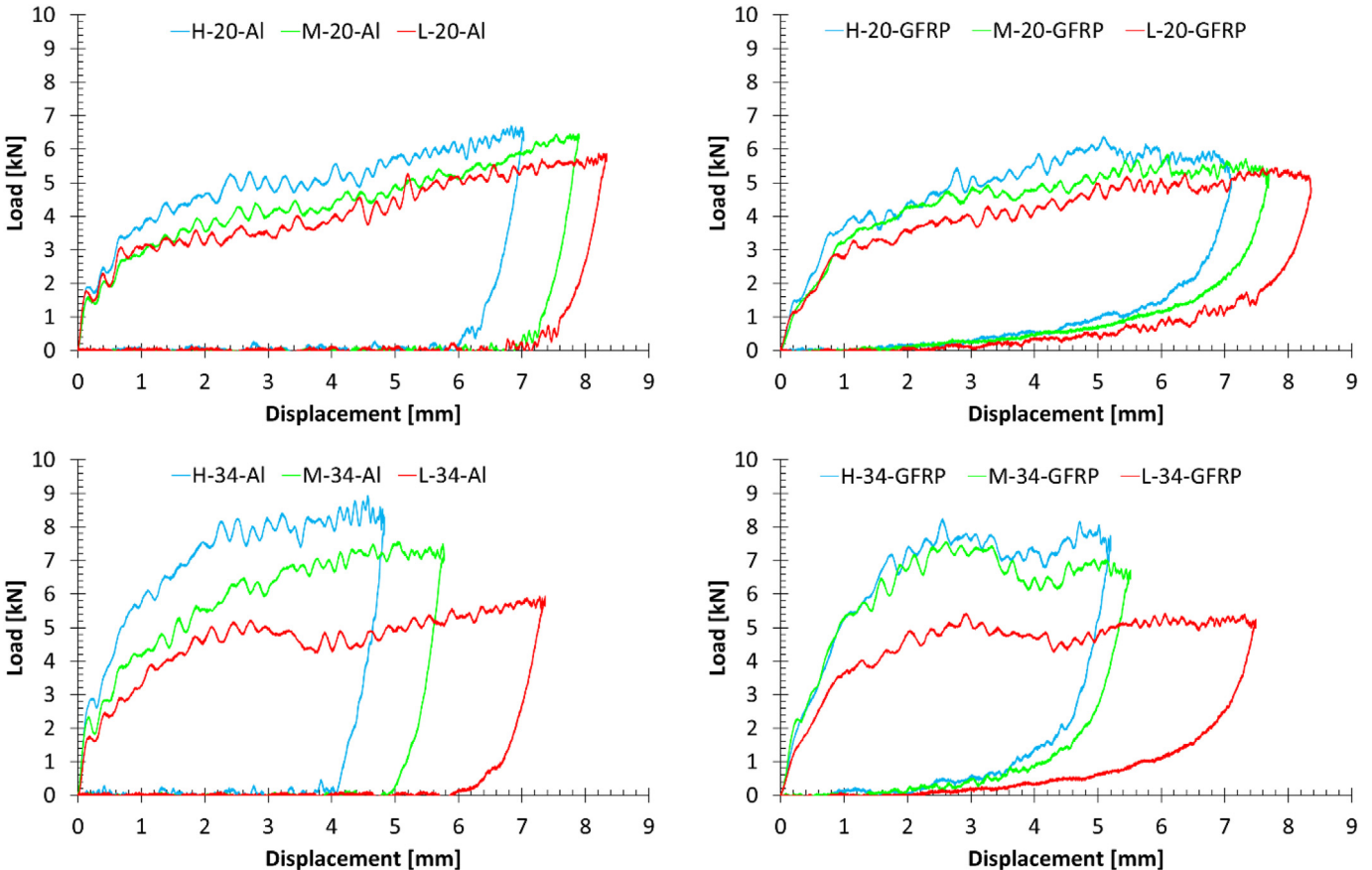


Fig. 8. Impact load-displacement curves for different sandwich-type samples.

Table 4
Impact test results.

Sample ID	D_x [N·mm]	T_{skin} [mm]	T_{core} [mm]	E_i [J]	F_{max} [N]	E_{ad} [J]	w [mm]	SAE [J/kg]
L-20-Al	$52.4 \cdot 10^3$	2	20	35	5875.9	31.9	8.3	667.8
M-20-Al			± 0.5	35	6461.1	32.7	7.9	657.4
H-20-Al				35	6701.0	32.0	7.0	573.5
L-34-Al	$56.7 \cdot 10^3$	4.3	34	35	5934.4	30.9	7.4	375.7
M-34-Al			± 0.5	35	7567.2	31.3	5.8	333.1
H-34-Al				35	8936.7	30.7	4.8	279.9
L-20-GFRP				35	5454.5	29.2	8.4	613.0
M-20-GFRP			± 0.3	35	5846.6	28.6	7.7	537.9
H-20-GFRP			35	6379.2	29.0	7.1	505.4	
L-34-GFRP			34	35	5425.2	28.6	7.5	373.7
M-34-GFRP			± 0.2	35	7561.4	28.6	5.5	316.9
H-34-GFRP				35	8246.1	28.6	5.2	281.5

design can transform the kinetic energy of projectile to irreversible plastic deformation. This merit will be further explained.

In order to observe the behaviour of projectile before, during and after impact, the kinetic energy during the impact is plotted versus time in Fig. 6b. It can be seen that the initial impact energy was 35 J and immediately after the initiation of contact with the absorber, this value decreases sharply down to zero. At this time, the majority of kinetic energy has been absorbed by the protective mechanism and the rebounding of the projectile is insignificant. The response of three foams was almost similar with minor differences in rebounding time. The relative difference between final and initial kinetic energy for H-50-Al-FEM is 82.2%, while this parameter for M-50-Al-FEM and L-50-Al-FEM is approximately equal to 86.2%.

The plastic dissipated energy of the absorbers is plotted in Fig. 6c in order to determine the magnitude of energy dissipated by irreversible plastic deformation during the impact. This parameter sharply increases in the response of projectile impact and reaches to its maximum value when the projectile velocity reaches to zero. The final plastic dissipated energy for M-50-Al-FEM and L-50-Al-FEM was higher than that of H-50-Al-FEM and equal to 25.15 J, which is 71.85% of the impact energy. The plastic dissipated energy for H-50-Al-FEM was 23.20 J, which is 8.4% lower than the other absorbers.

So far, it was observed that the performance of the absorbers with three different cores were almost similar. At the next step of design, the lighter panel L-50-Al-FEM was chosen. Then, there was the necessity to find the optimum thickness for the final design. As it was mentioned before, the allowable thickness of absorber can be up to 50 mm; however, the developed device can be designed slimmer. In order to find the optimum thickness for the absorber, the authors created a path of elements on the absorber on the axis of impact as depicted in Fig. 7. Afterwards, the final plastic deformation was plotted versus the location on the path. The impact energy is totally dissipated at the depth of 15 mm and there is 35 mm safe zone from which any of the absorbers did not undergo any deformation. Therefore, the final design of absorber can be thinner, and the thickness of minimum 20–35 mm can interestingly absorb the induced impact energy.

3.3. Low-velocity impact results

Low-velocity impact tests were carried out on all sandwich-type samples. In Fig. 8, the load-displacement curves for all tested sandwich panels are reported. By the comparison between samples with the same core thickness and skin material, the higher peak loads belong to the sample with the highest density. For a given thickness, aluminium skins present higher peak loads than GFRP ones.

A summary of impact tests results is reported in Table 4. For all samples, no complete failure of the aluminium foams was observed, since almost the entire impact energy was absorbed by the samples during tests. In particular, the energy transferred to the samples with

aluminium skins after impact was evaluated to 31.6 J, which represents 90.3% of the initial energy; while for the GFRP skins it was evaluated to 28.76 J, which represents 82.2% of the initial energy. For all samples, displacement decreased by increasing density; for a given skin material, it is higher in the samples with 20 mm thickness. From the results of the FE analyses, the minimum thickness of the absorber is within 20–35 mm. Thus, since sample with 20 mm thickness represents the minimum threshold, and by considering the core damage due to impact, the remaining useful material is too thin, as demonstrated in the following sections.

Among the samples with 34 mm thickness, those with the lowest density have the highest specific energy absorption values. In particular, samples with aluminium skins have higher energy absorbed values than GFRP ones. Furthermore, for economic reasons, ease of availability, atmospheric pollution due to production process, authors agreed that aluminium should be the best choice respect to GFRP as sandwich skin. Thus, in the sample tested, L-34-Al sample is considered the best choice. For a complete assessment of the different skins, a comparison was performed for NDE between the samples L-34-Al and L-34-GFRP (lowest density, 34 mm core thickness).

3.4. NDTs results

Visual inspection was used as first analysis method of the samples, in order to analyse the occurred damage. As expected, aluminium skin guarantees higher plastic deformation properties leading to a better energy transfer between skin and core. In Fig. 9 are reported all the samples tested during impact tests. Aluminium skin presents a more marked track than the GFRP and it is easier to detect the shape of the impactor (conical shape in this case). It can be seen that no failure or perforation of the skin occurs. The skin is locally bended in response of the impact and the sandwich panel absorbed impact energy through irreversible deformation [63–68].

GFRP skin does not present macroscopic deformation, the impact surface can be divided in a primary area where the impact occurred, and a secondary area affected by the impact. Shape and extent of the impact surface are difficult to detect for the GFRP due to the surface that usually is painted or covered with gel-coat; this can affect the measurements. Especially for the secondary area, the damage observed in visual testing does not match with the real damage detected by CT and shown below.

Optical microscopy was used as a second method of visual inspection to measure the impact area, for the GFRP only the primary area was considered. The measurements were carried out just for the samples with the lowest density on which the analyses were focused (Fig. 10). Aluminium skins present tracks with a more even pattern than GFRP skins, while the area measured is wider for samples with 20 mm core thickness.

CT was also applied on the sample with low core density in the investigation of the sample damage. The failure mechanism of the core is the same for all samples: collapse of the sandwich structures didn't appear, since no complete penetration of the cores was observed. In the zone just below the skin, densification of the cores was observed. CT was very helpful in the analysis of the samples with GFRP skin because the core damage is not easily detected from visual inspection due to the absence macroscopic deformation of the skin. The section of the L-20-GFRP sample in the middle layer is reported in Fig. 11a; the classic failure mechanism of the skin with conical shape damage was detected. This behaviour was more evident in the sample with lower thickness, because of the lower contribution of the core to support the external load. The local debonding between skin and core is not observable by visual inspection; the same behaviour was observed for the L-34-GFRP sample (Fig. 11d). Delamination was observed in the impact area (Figs. 11b); this behaviour cannot be detected by visual inspection as well. In particular, in Fig. 11c is visible the fracture of the laminae at the interface between skin and core (bottom layer of the

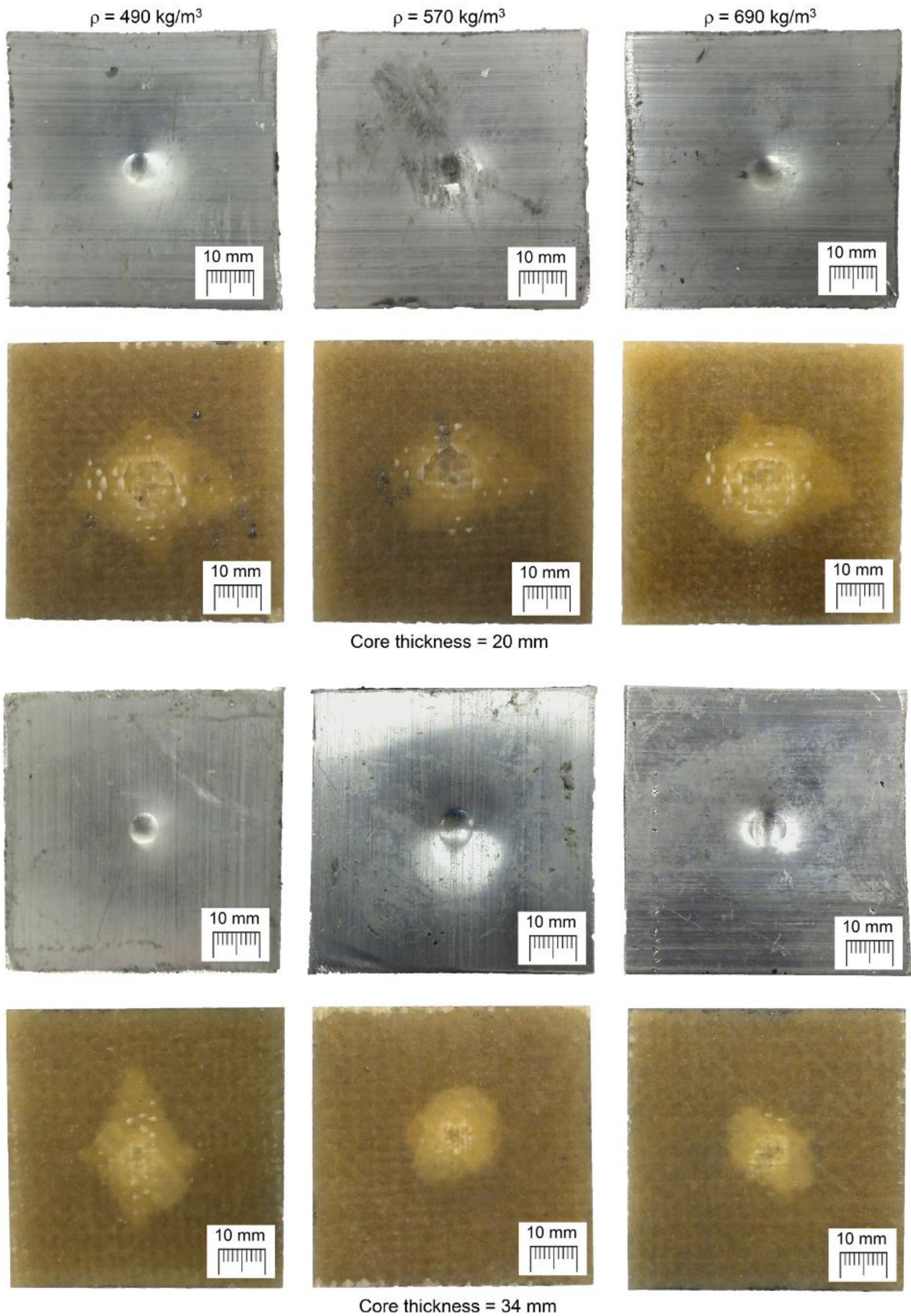


Fig. 9. Samples tested during impact tests.

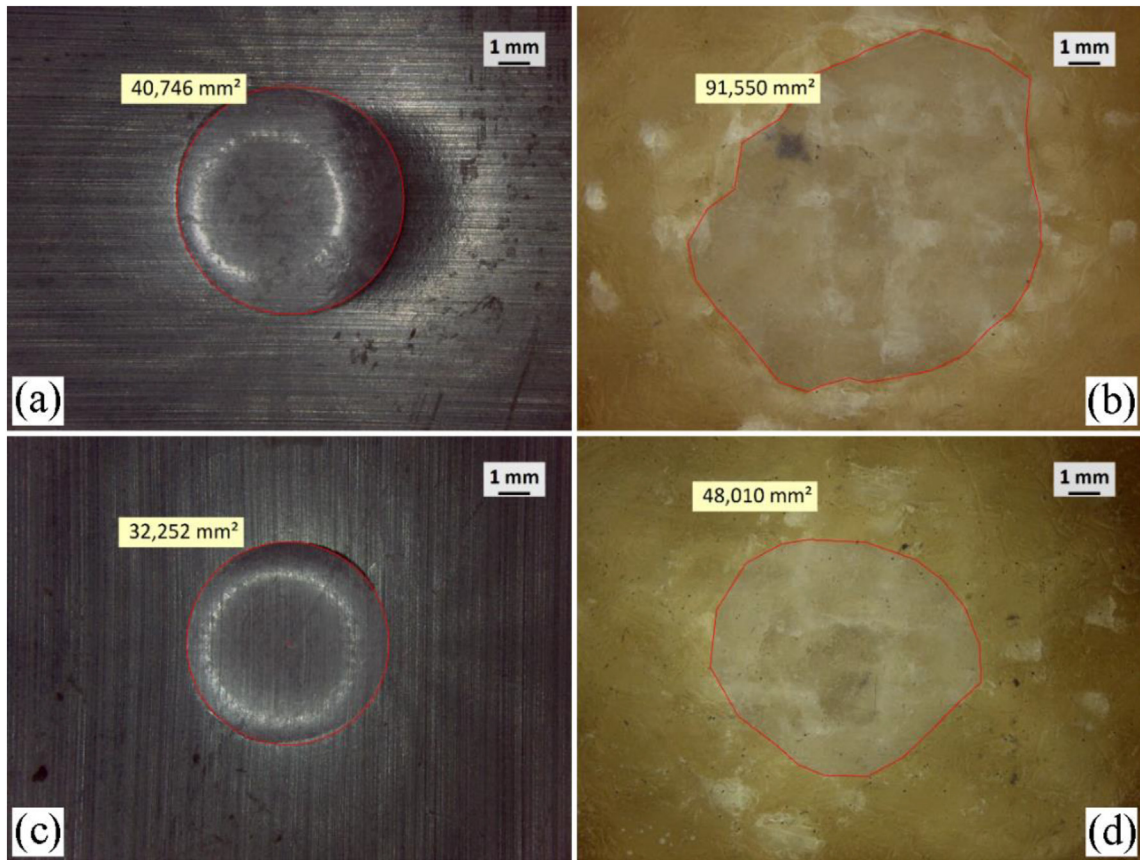


Fig. 10. Impact area of the tested samples: (a) L-20-Al; (b) L-20-GFRP; (c) L-34-Al; (d) L-34-GFRP.

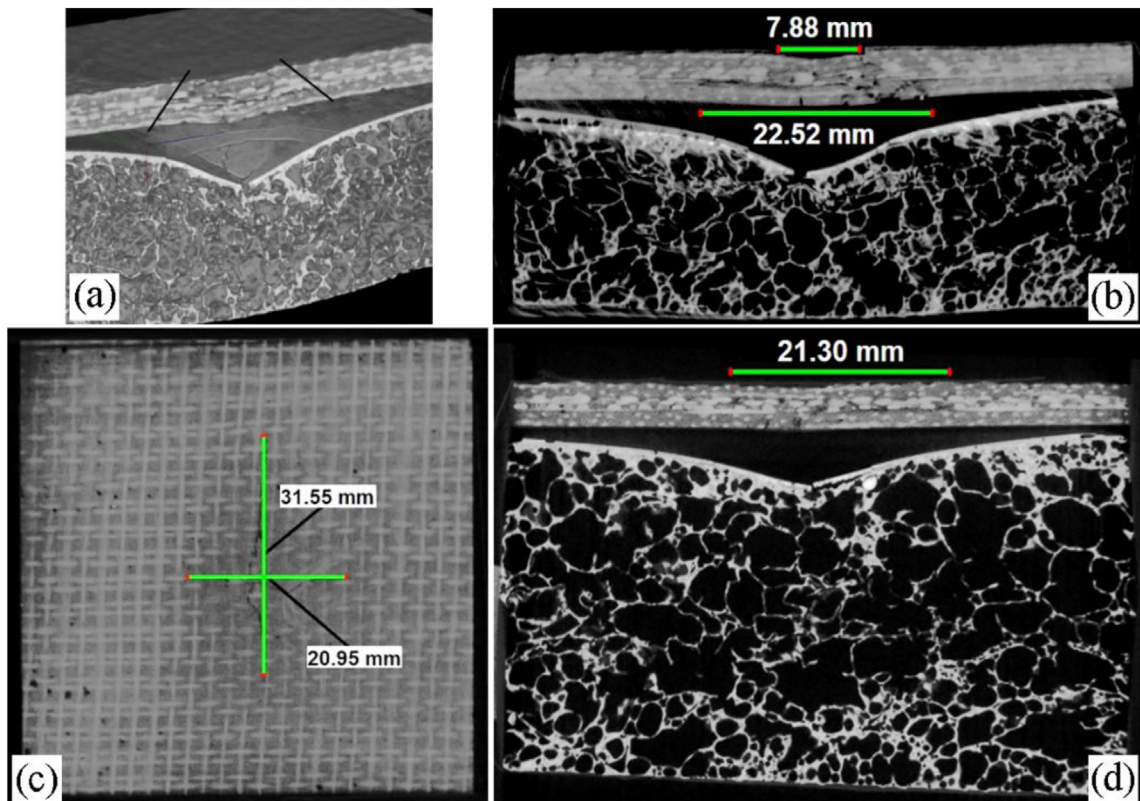


Fig. 11. 3D reconstruction (a) and orthogonal (b) of the mid-cross section of the L-20-GFRP sample; and tomogram of the skin (c) together with mid-cross section (d) of the L-34-GFRP sample.

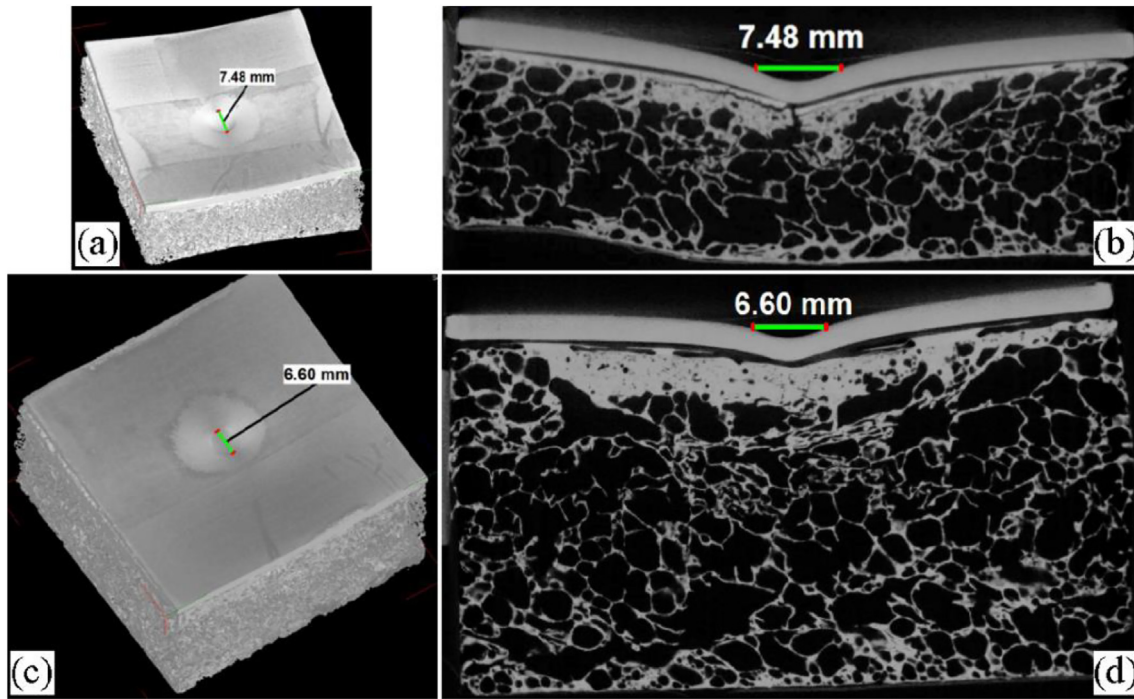


Fig. 12. 3D view (a) and mid-cross section (b) of the L-20-Al sample; and 3D view (c) together mid-cross section (d) of the L-34-Al sample.

skin); the fracture has a cross-shape and it follows the fibre direction, as CT image shows. The damage detection in longitudinal and transversal directions follows the trend observed by visual inspection (Fig. 9), even though the entity of the damage was underestimated by applying this NDT. Debonding of the GFRP skin was detected for all the samples, due to the inability of GFRP to follow plastic deformation of the aluminium foam core. Also, adhesive failure can be detected (Fig. 11a, b and d).

CT analyses of the samples with aluminium skin confirms the results obtained with other NDTs. Since the impact area can be approximated by a circular shape, by measuring its diameter both for L-20-Al and L-34-Al samples (Fig. 12a and c), the calculated area values are in accordance with those obtained with VT. The sample with 20 mm core thickness presents greater deformation of the skin, as visible in Figs. 12a and b, due to the lower contribution of the core in energy absorption. Moreover, in Fig. 12b the failure of the adhesive at skin-core interface can be detected; bending involved the whole volume of the specimen.

The damage appeared more localized for the thicker specimen, which also showed core densification just below impact area; in this case, adhesive failure occurred in a smaller area, which means that the efficiency of such specimen is higher in this specific experimental condition and, thus, for the proposed application.

From the UPA investigation, carried out on the samples with low core density, it was observed that NDT method was also useful in the analysis of the impact damage, since the obtained results matched with CT ones. In Fig. 13, the results obtained with UPA inspection are shown.

In Fig. 13a and b is reported a defect detected in a section in the skin of the L-20-GFRP sample; it is possible to observe that it matches with that observed in CT (Fig. 11b). In Fig. 13c is reported the C-Scan of the sample with the position of a severe damage due to delamination which are indicated in red according to the chosen palette. Considering that the impact position can be located in the centre of the specimen (the area in blue), it can be seen that delamination occurred in the area near the impact, due to the specimen bending.

For the sample L-34-GFRP, in Fig. 13d and e is depicted the damage detected during inspection. Also, in this case it is possible to observe that the results matched with CT inspection (Fig. 11d). UPA confirmed

that the damage was lower than that observed on sample L-20-GFRP, because of the higher contribute of the core in energy absorbing. This behaviour is particularly evident in C-Scan presented in Fig. 13f, if compared with C-Scan of the sample L-20-GFRP (Fig. 13c). Furthermore, in Fig. 13f is observable the damage presented in Fig. 13d due to a large delamination.

For samples with aluminium skin, as reported in section 2.2.3, the inspection was carried out on the whole sandwich structure. The obtained results show the damage on the core observed also with the other NDTs applied in this study. Moreover, zones where densification of the core occurred have been detected. In these zones, ultrasound can penetrate more easily than in the zones with high porosity where waves propagation is difficult due to the presence of air. Results of the inspection on the sample L-20-Al are shown in Fig. 13g, h and i. A core crushing of 9 mm and densification of the core was observed on the whole thickness of the aluminium foam in the impact zone, red parts in Fig. 13g. The analysed zone was the central part of the sample where the impact occurred as shown in Fig. 13i; from the C-Scan, the cracking of the adhesive can be observed, as already detected from CT analyses.

Core crushing on the sample L-34-Al is lower than the previous case due to the higher contribute of the aluminium foam in the impact energy absorption, as shown in Fig. 13l, m, n. The measured crushing in this case was 5 mm because of a better response of the core; this behaviour was confirmed by a lower presence of damage and irregularities than sample L-20-Al. Also, in this case the zone considered for the inspection was the central part of the sample (Fig. 13n).

By applying a very short thermal impulse of 4 kW with a flash, the damage of the fiberglass skins can be revealed. It is worth mentioning that a difference in the transient cooling down of the samples was evaluated by plotting the absolute temperature of the sound and the damaged areas, and the temperature difference. In the damaged zone of the sample with GFRP skin having a core thickness of 20 mm, a temperature increment of 3.6 °C was detected in the damaged zone, which is clearly visible in the thermograms in Fig. 14a. As revealed by CT analyses and UPA scans, the damage is more evident in the area near the impact point and has an apparent temperature higher than the nearest zones of the sample surface. The skin damage, mainly in terms of delamination

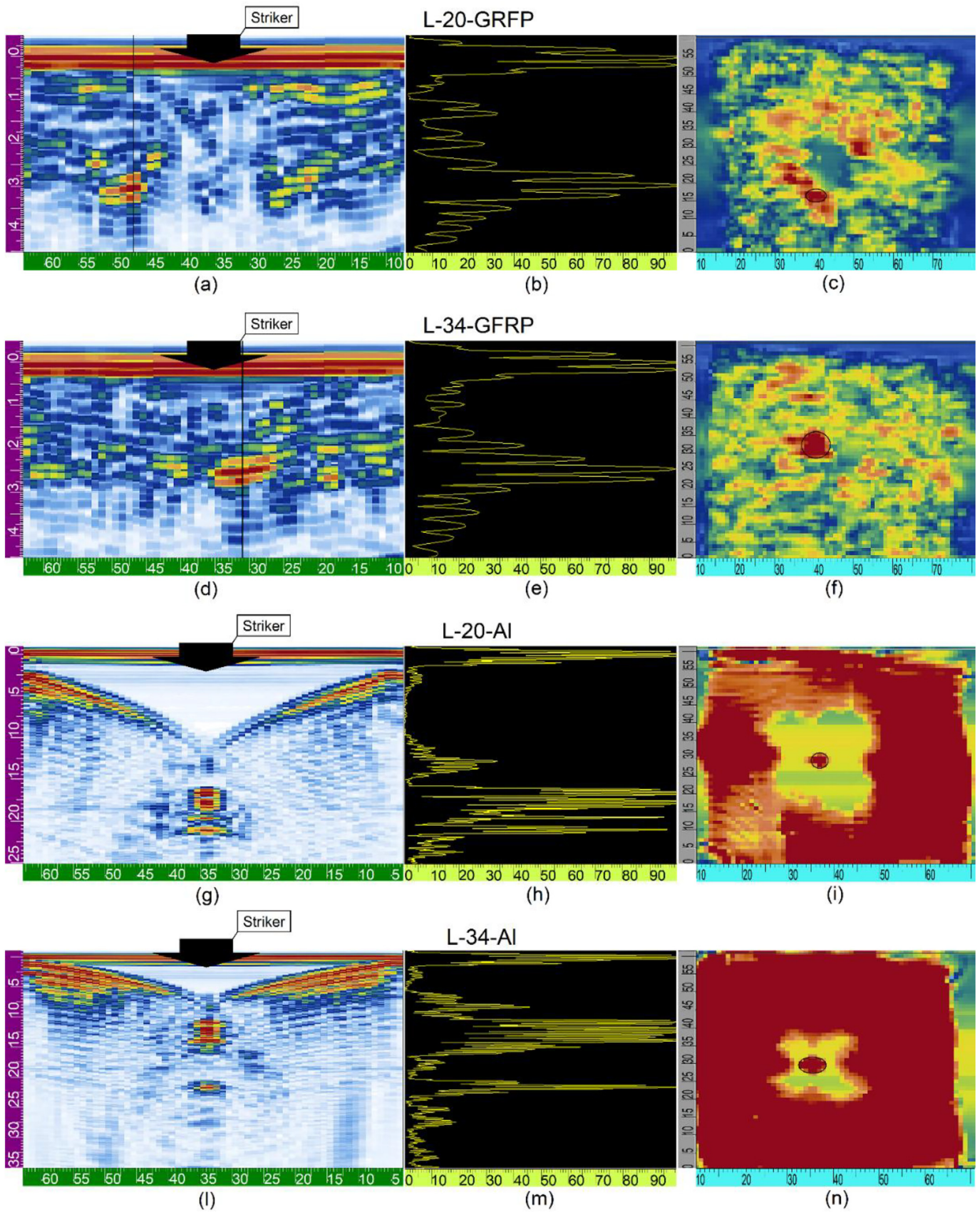


Fig. 13. A-Scan, B-Scan and C-Scan of the damage in UPA inspection: (a, b, c) L-20-GFRP; (d, e, f) L-34-GFRP; (g, h, i) L-20-Al; (l, m, n) L-34-Al.

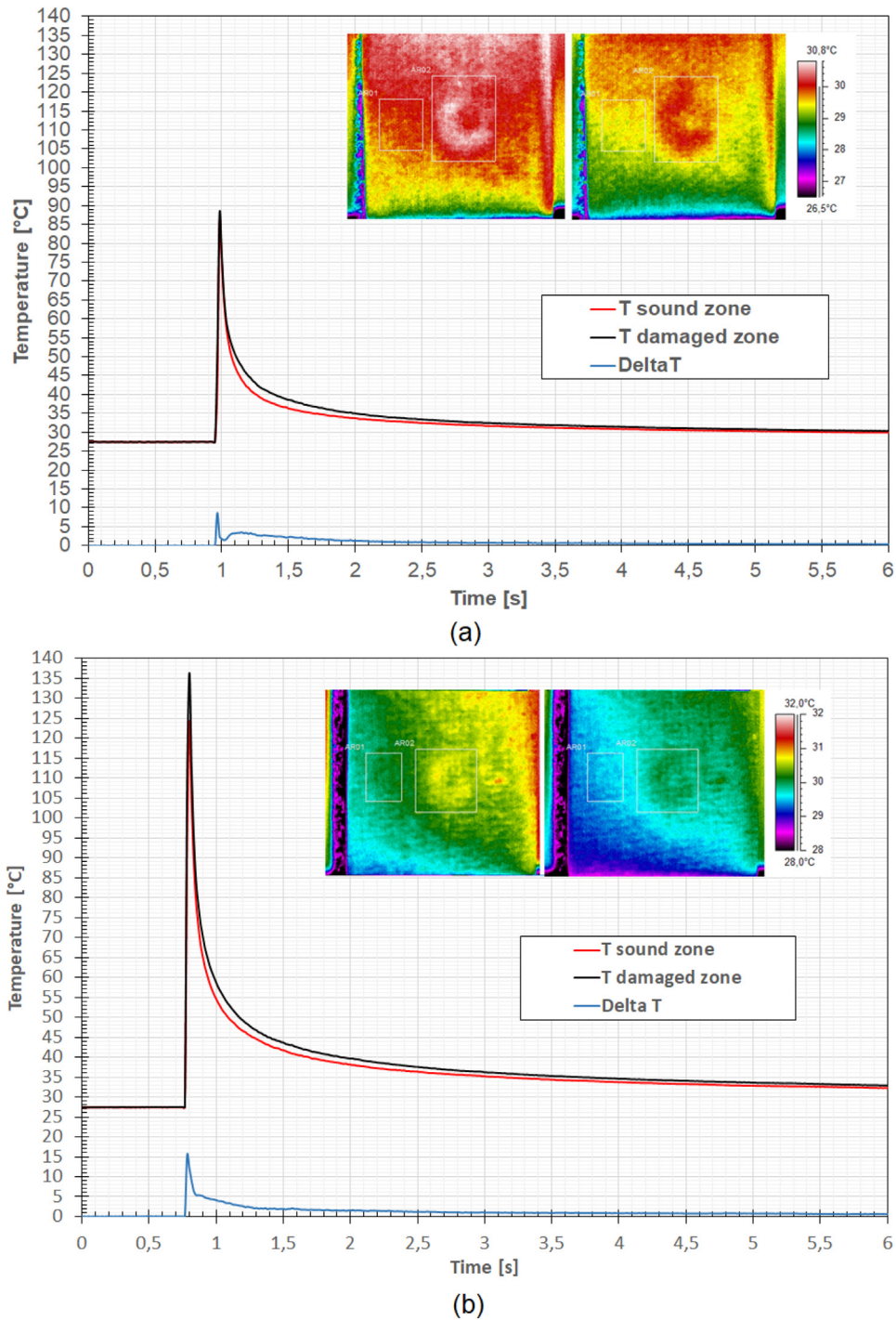


Fig. 14. Pulsed Thermography results of: (a) L-20-GFRP sample; (b) L-34-GFRP sample.

and fibre failure, causes a local change in conductivity, due to the presence of air; thus, damaged area appears with higher apparent temperature respect to sound zone. The different transient response is also due to the core thickness, which affects thermal properties at the skin-core interface.

In the samples having a core thickness of 20 mm, a slight delay can be seen in the temperature increment plot (Fig. 14a), due to the deeper damage of the skin, as already detected by other techniques and mainly due to the smaller thickness of the core, which is the main responsible of the energy absorption. For the samples having core thickness of 34 mm, the damage is barely visible in the thermograms. Temperature plot is

more useful to detect damaged area, as a temperature increment of about 5 °C can be locally found.

All NDT results can be summarized in the histogram in Fig. 15, showing the detected damage length. The damage length by UPA, for the specimens having Al skin, was evaluated in the B-scan considering the interface densified/undamaged zone in the core below the impact.

In Table 5 is reported which technique is reliable based on the analysed specimen. It can be realized that the inspection of the whole aluminium sandwich is easily to perform also with VT, for example in the daily maintenance; also, UPA is an effective technique for a deep inspection. The use of an encoder allows a rapid scanning inspection, with a

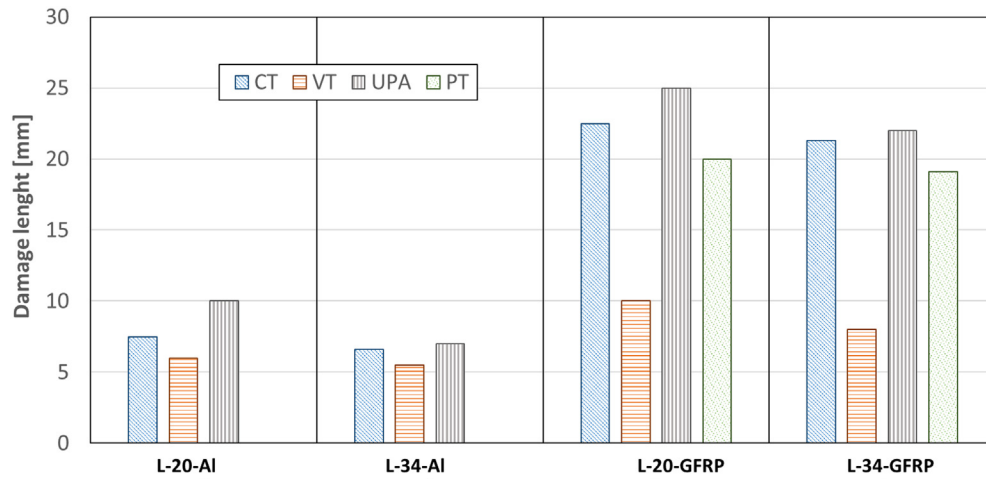


Figure 15. Summary of the results obtained from the applied NDTs.

Fig. 15. Summary of the results obtained from the applied NDTs.

precise location of the damaged area. It should be underlined that for GFRP skins, also PT is a reliable technique with the limit to detect damage only on the skin, even though the damage is slightly underestimated. Similar findings are reported in [19].

UPA in all analysed cases, slight overestimates the extension of the damage respect to CT technique, due to the lower resolution which cannot sharply separate sound area from damaged one [20]. UPA cannot resolve fibre fracture; thus, for specimens having GFRP skins, CT damage length in Fig. 15 is referred to delamination length.

4. Conclusions

In this paper, a novel flying ballast impact absorber device, called MFS (Metallic Foam Shell), is suggested to provide enough protection of railway vehicle axles and alleviate the complications of the conventional solutions. The investigations included sandwich panel materials with GFRP or Aluminium skin and different classes of closed-cell aluminium foam cores. The samples were manufactured and subjected to an extensive experimental campaign by compressive and low velocity impact tests. The quasi-static compressive tests were used for verification of a developed finite element model which allowed to estimate the behaviour of the device before choosing the final configuration.

In addition, an extended non-destructive evaluation by means of computed tomography, visual testing, ultrasonic phased array and pulsed thermography has been performed in order to find the most suitable technique for damage detection of the proposed device when on-service. Non-destructive evaluation allowed to assess that ultrasonic technique is the most reliable and effective to detect impact damage in both kinds of devices, even though the damage is slightly overestimated for GFRP skin; while is similar to computed tomography for the final design choice (whole aluminium sandwich structure). Considering that such technique is widely used in railway field, the inspections carried out for the maintenance of the axle can be also applied to the protective device without requiring an additional technique.

Table 5
Brief summary results. CT was considered as reference technique in the damage location.

NDT	Aluminium	GFRP
CT	✓	✓
VT	✓	✗
UPA	✓*	✓
PT	Not applicable	✓

Obviously, visual testing is suitable for both devices, with some complications for GFRP skin. Pulsed thermography can be a promising technique for fast detection of impact damage on GFRP skin and other high-emissivity devices already present in service, with a relative economic equipment. Due to the well-known reliability of computed tomography, in this research such technique was used to verify the response of the other techniques. The authors are aware that is impossible to apply CT for in-service inspections.

The suggested device can absorb impact energies through inelastic deformation, which is advantageous in terms of minimizing the rebounding of the ballast stones and impact recurrence. Low velocity impact tests showed that the suggested absorber can take up to 90% of the impact energy with total protection of the axle. Also, the samples with aluminium skins showed higher specific absorbed energy values than GFRP ones. Concerning the damage mechanisms due to impact event, non-destructive evaluation has shown that it was very localized for the device with aluminium skin, which didn't undergo to rupture; the core damage was mainly densification without perforation. Furthermore, for economic reasons, ease of availability, atmospheric pollution due to production process and recycling possibility it was concluded that aluminium should be the best choice for the skin of sandwich panel. It is worth mentioning that possible humidity can be isolated by interposing a cork sheet between the axle and the protective device to avoid galvanic corrosion occurrence.

A further step of this research is to produce a prototype of the device which takes in consideration the geometry of the axle. The proposed prototype is a foam-sandwich tubular component which will be tested at low velocity impacts.

Acknowledgments

This research was partially funded by a grant of the Romanian Ministry of Research and Innovation, project number 10PFE/16.10.2018, PERFORM-TECH-UPT—The increasing of the institutional performance of the Polytechnic University of Timisoara by strengthening the research, development and technological transfer capacity in the field of “Energy, Environment and Climate Change”, within Program 1—Development of the national system of Research and Development, Subprogram 1.2—Institutional Performance—Institutional Development Projects—Excellence Funding Projects in RDI, PNCDI III”. The authors are grateful to colleague Dr. Jaroslav Kováčik from the Slovak Academy of Sciences (Bratislava) for the preparation of foam panels.

Data availability

The raw data required to reproduce the findings of this work cannot be shared at this time as the data also forms part of an ongoing study.

Declaration of Competing Interest

The authors declare that they have no known competing financial interests or personal relationships that could have appeared to influence the work reported in this paper.

References

- [1] D. Klenam, et al., Exposure Time and Corrosion Behaviour of Typical South African Railway Axle Steels, 2017.
- [2] A. Zaremski, Fundamentals and Selected Technical Issues for High Speed and Heavy Axle Railroad Engineering, University of Delaware, 2017.
- [3] C. Locovei, M. Nicoră, On The Influence of Residual Stresses on Fatigue Fracture of Railway Axles, 2020.
- [4] A.P. Moon, et al., Passivation and corrosion behavior of modified Ferritic-Pearlitic railway axle steels, *J. Mater. Eng. Perform.* 24 (1) (2015) 85–97.
- [5] T. Makino, T. Kato, K. Hirakawa, Review of the fatigue damage tolerance of high-speed railway axles in Japan, *Eng. Fract. Mech.* 78 (5) (2011) 810–825.
- [6] A.T.S. Bureau, Derailment of XPT Passenger Train ST22, Harden, New South Wales, 9 February 2006, Australian Transport Safety Bureau, 2007.
- [7] D. Klenam, et al., Characterization of Railway Stock Axle Produced from Medium-Carbon Steel, 2015.
- [8] U. Zerbst, C. Klinger, D. Klingbeil, Structural assessment of railway axles – a critical review, *Eng. Fail. Anal.* 35 (2013) 54–65.
- [9] A.D. Quinn, et al., A full-scale experimental and modelling study of ballast flight under high-speed trains, *Proc. Inst. Mech. Eng. Part F J. Rail Rapid Transit.* 224 (2) (2009) 61–74.
- [10] R.A.M. Kenneth Earl Murphy, Gary Michael Nies, Protective device for a driving shaft, DE3569964D1, Deere and Co, Germany, 1984.
- [11] H.P. Camilla Kontio, Mats Karlsson, Protection for railway vehicle axle, US6568333B1, Bombardier Transportation GmbH, 2000.
- [12] H.L. Ulf Tolérus, Wheel axle cover, EP2345491A1, 2010, SJ AB.
- [13] E.K. Gilles Chretien, Alain Landrot, Method for Protecting an Axle of a Railway Vehicle, Corresponding Axle, and Bogie with Such an Axle, 2003 Alstom SA.
- [14] P.T. Thierry Guenard, Film for protection of axles, FR2881990A1, 2005, SNCF Mobilites.
- [15] P.T. Thierry Guenard, Claude Boccara, Annick Boccara née Houssin, Axle protection membrane, 2007 Fotia SNCF Mobilites: European Patent Office.
- [16] E.J. Steffen Dohn, Protection device for vehicle axle, DK177192B1, Danish Train Consulting Aps, 2010.
- [17] José Aitor Landaberea Rodríguez, M.A.I. Protector for rotary shaft of railway vehicles, WO2017203080A1, 2016, Construcciones Y Auxiliars De Ferrocarriles, S.A.
- [18] M.G. Ivanovich, V.G.M. G.V. Ivanovich, K.D. Aleksandrovich, S. V. Grigor'evich, Protective Device for rail Vehicle Wheel Pair Axle, 2020 RU2568001C1, Editor. 2014, Open Joint Stock Company Scientific Research and Design Technological Institute of Rolling Stock (JSC VNIKI).
- [19] P. Gaudenzi, et al., On the evaluation of impact damage on composite materials by comparing different NDI techniques, *Compos. Struct.* 118 (2014) 257–266.
- [20] A. Katunin, A. Wronkiewicz-Katunin, K. Dragan, Impact damage evaluation in composite structures based on fusion of results of ultrasonic testing and X-ray computed tomography, *Sensors* 20 (7) (2020) 1867.
- [21] D.P. Mondal, M.D. Goel, S. Das, Compressive deformation and energy absorption characteristics of closed cell aluminum-fly ash particle composite foam, *Mater. Sci. Eng. A* 507 (1) (2009) 102–109.
- [22] S. Sahu, et al., Low-velocity impact characteristics of closed cell AA2014-SiCp composite foam, *Compos. Part B* 160 (2019) 394–401.
- [23] P. Wang, et al., Effect of MWCNT content on conductivity and mechanical and wear properties of copper foam/resin composite, *Compos. Part B* 168 (2019) 572–580.
- [24] T. Voiconi, et al., Determination of flexural properties of rigid PUR foams using digital image correlation, *Solid State Phenom.* 216 (2014) 116–121.
- [25] E. Linul, L. Marsavina, J. Kováčik, Collapse mechanisms of metal foam matrix composites under static and dynamic loading conditions, *Mater. Sci. Eng. A* 690 (2017) 214–224.
- [26] N.V. Nguyen, J. Lee, H. Nguyen-Xuan, Active vibration control of GPLs-reinforced FG metal foam plates with piezoelectric sensor and actuator layers, *Compos. Part B* 172 (2019) 769–784.
- [27] A. Uzun, Production of aluminium foams reinforced with silicon carbide and carbon nanotubes prepared by powder metallurgy method, *Compos. Part B* 172 (2019) 206–217.
- [28] T.M. Pham, et al., Impact response and energy absorption of single phase syntactic foam, *Compos. Part B* 150 (2018) 226–233.
- [29] D.K. Rajak, et al., Fiber-reinforced polymer composites: manufacturing, properties, and applications, *Polymers* 11 (10) (2019) 1667.
- [30] H.J. Roven, et al., Mechanical properties of aluminium alloys processed by SPD: comparison of different alloy systems and possible product areas, *Mater. Sci. Eng. A* 410–411 (2005) 426–429.
- [31] P. Corigliano, et al., Experimental and theoretical analyses of Iroko wood laminates, *Compos. Part B* 112 (2017) 251–264.
- [32] J.N. Reddy, Theory and Analysis of Elastic Plates and Shells, CRC Press, 2006.
- [33] Standardization, I.O.F., Mechanical testing of metals - Ductility testing - Compression test for porous and cellular metals, ISO13314, 2011.
- [34] A. Sakly, et al., Experimental and modelling study of low velocity impacts on composite sandwich structures for railway applications, *Eng. Fail. Anal.* 68 (2016) 22–31.
- [35] ASTM, Standard Test Method for Impact Resistance of Flat, Rigid Plastic Specimens by Means of a Falling Dart (Tip or Falling Mass), 2018 West Conshohocken, PA.
- [36] H. Mozafari, et al., In plane compressive response and crushing of foam filled aluminium honeycombs, *J. Compos. Mater.* 49 (26) (2014) 3215–3228.
- [37] H. Mozafari, et al., Finite element analysis of foam-filled honeycomb structures under impact loading and crashworthiness design, *Int. J. Crashworthiness* 21 (2) (2016) 148–160.
- [38] V.S. Deshpande, N.A. Fleck, Isotropic constitutive models for metallic foams, *J. Mech. Phys. Solids* 48 (6) (2000) 1253–1283.
- [39] U. Zerbst, et al., The development of a damage tolerance concept for railway components and its demonstration for a railway axle, *Eng. Fract. Mech.* 72 (2) (2005) 209–239.
- [40] V. Crupi, G. Epasto, E. Guglielmino, Comparison of aluminium sandwiches for light-weight ship structures: Honeycomb vs. foam, *Mar. Struct.* 30 (2013) 74–96.
- [41] M.A. Hazizan, W.J. Cantwell, The low velocity impact response of an aluminium honeycomb sandwich structure, *Compos. Part B* 34 (8) (2003) 679–687.
- [42] D. Feng, F. Aymerich, Damage prediction in composite sandwich panels subjected to low-velocity impact, *Compos. A: Appl. Sci. Manuf.* 52 (2013) 12–22.
- [43] E. Linul, N. Movahedi, L. Marsavina, On the lateral compressive behavior of empty and ex-situ aluminum foam-filled tubes at high temperature, *Materials (Basel, Switzerland)* 11 (4) (2018) 554.
- [44] K. Myers, et al., Quasi-static and high strain rate response of aluminum matrix syntactic foams under compression, *Compos. A: Appl. Sci. Manuf.* 79 (2015) 82–91.
- [45] A. Ghazi, et al., Multiscale computational modelling of closed cell metallic foams with detailed microstructural morphological control, *Int. J. Eng. Sci.* 143 (2019) 92–114.
- [46] Y. Solyaev, et al., On a combined thermal/mechanical performance of a foam-filled sandwich panels, *Int. J. Eng. Sci.* 134 (2019) 66–76.
- [47] D. Muchala, et al., Effect of SWCNTs content and relative density on the energy absorption capabilities of closed-cell Al-cenosphere-SWCNTs hybrid foam, *Compos. Part B* 176 (2019) 107304.
- [48] C.S. Roszkos, et al., Static and dynamic analyses of aluminum foam geometric models using the homogenization procedure and the FEA, *Compos. Part B* 171 (2019) 361–374.
- [49] N. Movahedi, et al., Functionally graded metal syntactic foam: fabrication and mechanical properties, *Mater. Des.* 168 (2019) 107652.
- [50] G. Sun, et al., Low-velocity impact behaviour of sandwich panels with homogeneous and stepwise graded foam cores, *Mater. Des.* 160 (2018) 1117–1136.
- [51] A. Szlancsik, et al., Compressive behavior and microstructural characteristics of iron hollow sphere filled aluminum matrix syntactic foams, *Materials* 8 (2015) 7926–7937.
- [52] J. Kováčik, et al., Scaling of compression strength in disordered solids: metallic foams, *Frattura ed Integrità Strutturale* 36 (2016) 55–62.
- [53] T.M.J. Gebhart, et al., Multi-scale modelling approach to homogenise the mechanical properties of polymeric closed-cell bead foams, *Int. J. Eng. Sci.* 145 (2019) 103168.
- [54] A.D. Akinwékomi, et al., Synthesis and characterisation of floatable magnesium alloy syntactic foams with hybridised cell morphology, *Mater. Des.* 160 (2018) 591–600.
- [55] I.N. Orbulov, et al., Compressive mechanical properties of low-cost, aluminium matrix syntactic foams, *Compos. A: Appl. Sci. Manuf.* 135 (2020) 105923.
- [56] E. Linul, et al., Compressive properties of zinc syntactic foams at elevated temperatures, *Compos. Part B* 167 (2019) 122–134.
- [57] E. Linul, et al., Cryogenic and high temperature compressive properties of metal foam matrix composites, *Compos. Struct.* 209 (2019) 490–498.
- [58] G. Kırmızı, H. Ank, H. Çinici, Experimental study on mechanical and ballistic behaviours of silicon carbide reinforced functionally graded aluminum foam composites, *Compos. Part B* 164 (2019) 345–357.
- [59] D. Chen, L. Jing, F. Yang, Optimal design of sandwich panels with layered-gradient aluminum foam cores under air-blast loading, *Compos. Part B* 166 (2019) 169–186.
- [60] G.H. Acker, Protective mechanism for variable, US2675713A, Cleveland Worm & Gear Company, USA, 1954.
- [61] H. Mao, R. Rumpel, P. Göransson, An inverse method for characterisation of the static elastic Hooke's tensors of solid frame of anisotropic open-cell materials, *Int. J. Eng. Sci.* 147 (2020) 103198.
- [62] L. Li, et al., Shock loading simulation using density-graded metallic foam projectiles, *Mater. Des.* 164 (2019) 107546.
- [63] H. Fan, et al., Approaching perfect energy absorption through structural hierarchy, *Int. J. Eng. Sci.* 130 (2018) 12–32.
- [64] Q. Huang, et al., An efficient approach for post-buckling analysis of sandwich structures with elastic-plastic material behavior, *Int. J. Eng. Sci.* 142 (2019) 20–35.
- [65] J. Crespo, F.J. Montáns, General solution procedures to compute the stored energy density of conservative solids directly from experimental data, *Int. J. Eng. Sci.* 141 (2019) 16–34.
- [66] L.P. Maiorano, J.M. Molina, Challenging thermal management by incorporation of graphite into aluminium foams, *Mater. Des.* 158 (2018) 160–171.
- [67] T. Wejrzanowski, et al., Metallic foam supported electrodes for molten carbonate fuel cells, *Mater. Des.* 193 (2020) 108864.
- [68] W. Zhai, et al., Microstructure-based experimental and numerical investigations on the sound absorption property of open-cell metallic foams manufactured by a template replication technique, *Mater. Des.* 137 (2018) 108–116.